

Research Article

Solar GHI Ensemble Prediction Based on a Meteorological Model and Method Kalman Filter

Yuanyuan Liu 

Department of Mathematics, Luliang University, Luliang 033001, China

Correspondence should be addressed to Yuanyuan Liu; hnzykys@126.com

Received 15 April 2022; Revised 20 May 2022; Accepted 21 May 2022; Published 10 June 2022

Academic Editor: Upaka Rathnayake

Copyright © 2022 Yuanyuan Liu. This is an open access article distributed under the Creative Commons Attribution License, which permits unrestricted use, distribution, and reproduction in any medium, provided the original work is properly cited.

The intensity of light emanating from sun is determined by using a meteorological version and is altered with the numerical version, and the forecast accuracy is improved in advance by using Kalman Filter. As the accuracy of the version output related to its specific position is often questionable, group prediction constituting three members is suggested and agreed upon measurement. Also, this ensemble prediction provides an estimation of the solar global horizontal irradiance uncertainty (i.e., coverage rate of the prediction interval), which can be useful to provide flexible energy production forecasts. This article displays how the method Kalman filter could be used as an error correction way to alter the predicted irradiance value. The Kalman filter ameliorates the prediction of solar global horizontal irradiance as well as its interval. As the empirical coverage rate increases and closes to the nominal coverage rate, the interval size reduces.

1. Introduction

Having been installed and connected to power grids, a large amount of photovoltaic (PV) systems with their prognostication in power generation or the prediction of the solar irradiance have been used in handling the electric grids more efficiently to make the energy provision steadier. With the help of dependable and conforming prediction data [1–9], system operators ameliorate the electrical management to balance the users and power generation [10–12]. Also, with the development of the forecasting models, support is offered in an efficient way for electricity suppliers in managing, dispatching, and planning power plants [13]. By applying a meteorological model, the authors have advanced a system in ensemble prediction of solar global horizontal irradiance [14], and not only the irradiance but also its prediction interval has been forecasted [15–17]. The interval corresponds to the reliability of the forecasting and will be also useful for power grid management. With the use of model WRF (the Weather Research and Forecasting), Liu et al. proposed solar global horizontal irradiance and verified its forecasting accuracy [14]; the simulated WRF irradiance included RMSEs, which imply root mean square errors

[18–26] as well as positive biases. In order to improve solar global horizontal irradiance forecasting accuracy, the meteorological calculation used in a post-processing technique is introduced [27–30]; and, the result in the amelioration on the forecasting of the prediction interval is also discussed in this work [31–34].

Different approaches for processing in post-period, with examples of MOS (model output statistics) [35–39] and Kalman filter, are put into use in weather forecast in a frequent way for the sake of modifying the anticipatory output in gaining possession by NWP models which stand for numerical weather prediction. In 1995, Homleid depicted a model Kaman Filter to estimate temperature forecasting corrections in day time [34]. In 2011, De Carvalho et al. [35] applied the model Kalman filter for correcting the mean temperature errors which are assessed by the model PRECIS, a system developed by the English Hadley Centre used for climate predictions in regional area. In 2008, Monache et al. [36] estimated systematic errors in surface ozone forecasts. Galanis et al. in 2006 [37] as well as Cassola and Burlando in 2012 [38] put the method Kalman filtering procedure into removing bias in forecasting for wind speed. Pelland et al. in 2013 [39] as well as Diagne et al.

in 2014 [40] used the model Kalman filter to remove bias in solar irradiance prediction. In 2018, Rincón with his teammates [41] made a combination with model Kalman filter and MOS for bias correction for the sake of improving the entire predicted values in solar irradiance. The creation of correction function method on linear regression traditionally depends mainly on MOS. According to Kalman [42] and Homleid [34], the theory of the Kalman filter offers equations in modifying the assessments in a recursive way through observing.

The probabilistic forecasting of solar global horizontal irradiance can have an important impact on the management of the power grid with many PV systems and its risk analysis. For this case, the method Kalman filter is used as a posttreatment technique to rectify the system flaws of prediction of solar gleam and, on the other hand, influences the development on anticipating the gauge interval employing a group anticipating approach also inspected.

2. Meteorological Model and Solar Global Horizontal Irradiance Forecasting

2.1. Model WRF Configuration. As is shown previously in the research work [14], the performance with the WRF model, which means Weather Research and Forecasting by Skamarock et al. 2008 [43], was supervised from July 2013 to June 2014 for the prediction of inexhaustible energy resources, for example photovoltaics or wind power generations [44–47]. The model WRF is also applied in an extensive way, for the reason that it can be used to simulate the weather in reality with the technique of high resolution. The calculation back drop of meteorology with WRF are summed up in Table 1.

The simulation was driven based on the analysis of data in a global scope for the GSM-JP standing for area of Global Spectral Model for Japan. The spatial resolution of the analyses was $0.2^\circ \times 0.25^\circ$, while the temporal resolution was 3 h. The WRF exemplary composition constitute three consecutive installed realms with 18 kilometers of grid spacing, which is the grid in coarser style showed in domain 1 [48]. Also, the 6 kilometers of grid spacing will be showed in domain 2 and 2 kilometers of grid spacing is in domain 3, which is the best grid, accompanied with 50 vertical levels. Estimates which correspond to the most inside domain grid points (domain 3) enclosing the stations of experimental radiometric were put into use in the assessment.

Physical parameterizations in a wide range are enclosed in the model WRF, allowing setting the WRF model to depict the physical processes in a better way which are based on resolution, model domain, application, and location. Under such circumstances, various problems were chosen to pursue. Shimada et al. [49] supervised an assessment study of the achievement of distinct problems of the exemplary in the identical researching field.

Thus, the model WRF was functioned with the MYJ planetary boundary layer scheme [50], the Betts-Miller-Janjic cumulus scheme [51], WSM 6 microphysical scheme [52], the Noah land surface model, the scheme of Dudhia for shortwave radiation scheme [53], and the RRTM scheme for

long-wave radiation scheme [54]. With regard to every day, a 3-day (72 h) ahead prediction was fulfilled, which started at 12 h Universal Coordinated Time (UTC).

2.2. Study Area and Observed Data. The central region of Japan is the study field for the solar global horizontal irradiance prediction; the research area includes Aichi, Nagano, Mie, Shizuoka, and Gifu Prefectures. Results of the present research have been assessed with the observation data which are collected at 61 radiometric observation stations displayed in Figure 1. The main reasons why these stations are chosen is because they are located near to regions where the solar power plants are running or under construction. The solar global horizontal irradiance (GHI) data were collected by EKO pyranometer MS-402 in these stations. In this research, to get data in 30 minutes, measurements in 10 seconds were averaged. Moreover, since researches were operated in one field where the commercial electric power grid locates, the GHI averaged data for GHI from all 61 stations of Figure 1 are used for the assessment. The data at night, which refer to time period from sunset in the previous day to sunrise in the intraday time, are excluded from the assessment [55–57].

2.3. Forecasted Results with WRF. With the method Kalman filter as a posttreatment technique of solar global horizontal irradiance, calculation by model WRF is correlated with the checked information. As is explained before, the solar GHI averaged values over 61 stations in the Figure 1 and with 30-minute frequency is used for the checking. The data at night are not used for the evaluation.

Figure 1 shows correlation charts between the forecasted solar global horizontal irradiance and the observation from the beginning in July 2013 to the end of June in 2014. Such statistical error indexes as biases, root mean square errors, and correlation coefficients, which are abbreviated as Bias, RMSE, and CORR respectively, are listed in Table 2. The WRF computes 72-h ahead forecasting in one operation, which includes the intraday $M_{i,0}$, the next-day $M_{i,1}$ and the 2-day ahead $M_{i,2}$ prediction. Subscript i indicates operation day of the forecasting. The labels “ $M_{i,j}$ ” only refers to the simulated GHI with model WRF, and “ $M_{i,j} - \text{KF}$ ” refers to the result which is adjusted with method Kalman filter. The outcomes are studied separately for $M_{i,0}$, $M_{i,1}$, and $M_{i,2}$ forecasting in this figure and this table. For the same target day, the ensemble average value is computed as a mean of the members, which consist of $M_{i,0}$, $M_{i-1,1}$, and $M_{i-2,2}$, standing for the very day forecasting in the operation day i .

3. Kalman Filter for Improvement of WRF Forecasting

3.1. Method Kalman Filter. Designed to collect a signal in an efficient way from data in noisy environment that consists of statistical noise and other inexact ones, Kalman filter method is therefore expected to show a more exact outcome by using training data [40, 58, 59]. This approach is ordinarily employed to rectify systems flaws of weather forecast

TABLE 1: Configuration of the WRF model.

Input data	JMA GSM-JP (3-hourly, $0.2^\circ \times 0.25^\circ$) NCEP GFS (3-hourly, $0.5^\circ \times 0.5^\circ$)
Vertical layer	50 levels (surface to 100 hPa)
Nesting	2-way nesting
Domain	Domain 1, D01 (18 km, 120×110 grids), domain 2, D02 (6 km, 130×130 grids), and domain 3, D03 (2 km, 160×229 grids)
Physical options	Mellor-Yamada-Janjic PBL parameterization Betts-Miller-Janjic cumulus parameterization WSM 6-class graupel scheme Dudhia short wave radiation scheme RRTM long wave radiation scheme (domain 1 and domain 2 only) Noah land surface model

further and has been ratified as one of establishment approach of meteorology forecast supervision; such meteorological parameters as amount of precipitation, temperature, and probability of precipitation are studied based on this method, according to Kunitsugu [60]. The application of Kalman filter in the meteorological field is different from other fields. The correction coefficient of the observation and prediction error of solar irradiance are obtained, not physical quantities. Compared with other methods, Kalman filter is not so complex and is suitable for the solar GHI forecasting corrections. Meanwhile, the Kalman filter has not been widely applied in this field before. Also, the results of Kalman filter could be realized by MATLAB efficiently and conveniently.

By and large, previous values before the time k have an effect on the arbitrary instantaneous k time value to some extent. The method Kalman filter follows a trail of the previous data as the state of the system and renews it with the observation value. The Kalman filter method usually contains observation equations and state equations.

$$z_k = Hx_k + v_k, \quad (1)$$

$$x_k = Ax_{k-1} + w_k. \quad (2)$$

On the basis of state equation, equation (1), it is assumed in Kalman filter that the state at time k is generated from the previous one at time $k-1$. In equation (2), x_k refers to a state variable, A refers to a state transition matrix, and w_k refers to a state transition noise. On the basis of observation equation, equation (1), the observation data z_k is computed by utilizing the state variable x_k . H refers to a state-to-observation matrix and v_k means the noisy data in the observation. It is assumed that noise plays a key role in method Kalman filter. The two white noises w_k and v_k are compliant with Gaussian zero mean.

Figure 2 displays the calculation flow in Kalman filter algorithm which is described as equations, referring to Kim and Huh [61]. The first step is to set the initial values, which include the error covariance matrix P_0 , an internal variable initial value, and evaluated state variable \hat{x}_0 . Then, the estimated state variable \hat{x}_k at time k is evaluated and updated with the observation data z_k by following the algorithm.

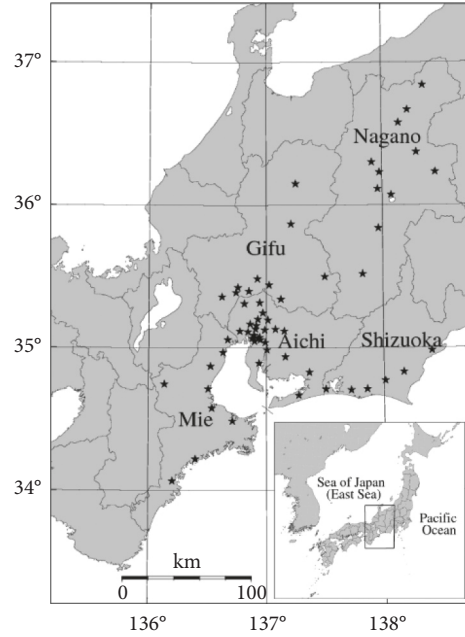


FIGURE 1: Study region and distribution of the radiometric stations with global irradiance measurements (dark stars).

In this case, we make use of the method Kalman filter to correct the unfairness of the predicted solar global horizontal irradiance in accordance with the system flows of prediction. Predicting the future bias by using a linear relationship between the estimated previous bias present and the forecasting error, Kalman filter is such a mathematical approach [49]. After the estimation of current bias, to ameliorate the forecasting, it is detached from the solar global horizontal irradiance which is forecasted with model WRF. It is assumed that, the simulated solar global horizontal irradiance with model Kalman filter is assessed from forecasted GHI based upon model WRF according to the following equation:

$$\hat{I}_{\text{WRF}} = aI_{\text{WRF}} + b, \quad (3)$$

where a and b are correction coefficients. On this assumption, the state variable is defined as $x_k = (a \ b)^T$. Also, the observation equations and the state corresponding to equations (1) and (2) can be inferred in the following equations.

TABLE 2: Statistical indexes for solar GHI different forecasts.

Forecasting method and member	Bias [W/m^2] (Relative bias)	RMSE [W/m^2] (Relative RMSE)	CORR [-]
$M_{i,0}$	49.7 (28.8%)	102.9 (59.6%)	0.950
$M_{i,0}$ - KF	-2.4 (-1.4%)	79.1 (45.8%)	0.951
$M_{i,1}$	51.4 (29.7%)	118.9 (68.9%)	0.929
$M_{i,1}$ - KF	-6.0 (-3.5%)	94.6 (54.7%)	0.930
$M_{i,2}$	50.8 (29.4%)	129.8 (75.2%)	0.911
$M_{i,2}$ - KF	-8.5 (-4.9%)	106.6 (61.7)	0.911
Ensemble mean	50.6 (29.3%)	104.9 (60.7%)	0.946
Ensemble mean-KF	-5.6 (-3.2%)	81.8 (47.4%)	0.947
Persistent	0.3 (0.15%)	191.7 (110.9%)	0.718

$$z_k = Hx_k + v_k, \quad (4)$$

$$= (I_{\text{WRF}} \ 1) \begin{pmatrix} a \\ b \end{pmatrix}_k + v_k,$$

$$x_k = Ax_{k-1} + w_k, \quad (5)$$

$$= \begin{pmatrix} 1 & 0 \\ 0 & 1 \end{pmatrix} \begin{pmatrix} a \\ b \end{pmatrix}_{k-1} + w_k,$$

where $z_k = \hat{I}_{\text{WRF}}$. With regard to the function of Kalman filter, v_k in the equation (4) and its relevant covariance matrix R , and w_k in the equation (5) and its relevant covariance matrix Q in the equations Figure 2 are essential impact factors. To perform different WRF simulations, various matrices R and Q are input to gain their appropriate values. Figure 3 displays the solar GHI's RMSE during the intraday forecasting under different matrices R and Q , which reduce the predicted RMSE. According to Figure 3, the adequate rate between the impact factors R and Q could be found out. From this result, we gain that R is equal to $1 \times 10^{11.5}$ and Q is equal to $1 \times 10^0 \begin{pmatrix} 1 & 0 \\ 0 & 1 \end{pmatrix}$.

The time series of the correction coefficients a and b in the equation (3) is displayed in Figure 4. Compared with the solar GHI's order about 100 or $1,000 \text{ W/m}^2$, b can be ignored. From this figure, b increases over time, and a varies by season. In the filter, the two coefficients vary with time, working to regulate the solar global horizontal irradiance which is predicted with Model WRF.

3.2. Forecasting Results with WRF and Kalman Filter. Figure 5 shows correlation diagrams of the observed GHI and the forecasted data. Ensemble means shown in Figures 5(g) and 5(h) are irradiances averaged in the same target day. Also, the persistent model as a reference one is

displayed in Figure 5(i). Table 2 enlists scientific mistakes indices of weather prediction. Both of the results in CORRs and RMSEs based on model WRF forecasts are superior to those which are acquired by the persistent model. The validity of the forecasting with model WRF are uncovered in this result. But the bias value of model WRF forecasts is larger than that of the persistent model, which is zero in theory.

Biases of $M_{i,0}$, $M_{i,1}$ and $M_{i,2}$ forecasting by using model WRF are 49.7 W/m^2 , 51.4 W/m^2 , and 50.8 W/m^2 , respectively. According to these outcomes, a notable positive bias is found in the solar GHI forecasting with model WRF, which signifies that the solar GHI with WRF model is overestimated [62–65].

As found in this figure and this table, the bias values are decreased clearly by utilizing the method Kalman filter; for instance, with the help of method Kalman filter, the bias of $M_{i,0}$ forecasting turns from 49.7 W/m^2 to -2.4 W/m^2 . By comparing with the solar irradiance mean intensity, the biases could be practically negligible. With the use of method Kalman filter, the two indices RMSEs and biases decrease while CORRs raise as is shown in Table 2. Those relative RMSEs and biases in this table are normalized with their mean values. These relative indices are also improved by applying Kalman filter. The function of the method Kalman filter to the forecast precision is proved with the amelioration of these indices.

The correction coefficient a of the Kalman filter in Figure 4 is nearly 0.88, and smaller than unity. The method Kalman filter decreases the solar global horizontal irradiance intensity which is predicted with model WRF and rectifies the overestimation of model WRF output with the value a .

The intraday forecasting of daily operation is associated and stated in the form of time series in Figure 6. The observed solar global horizontal irradiance is also plotted in this figure. The irradiance which is forecasted with model WRF seems a little greater than the measured one, but after

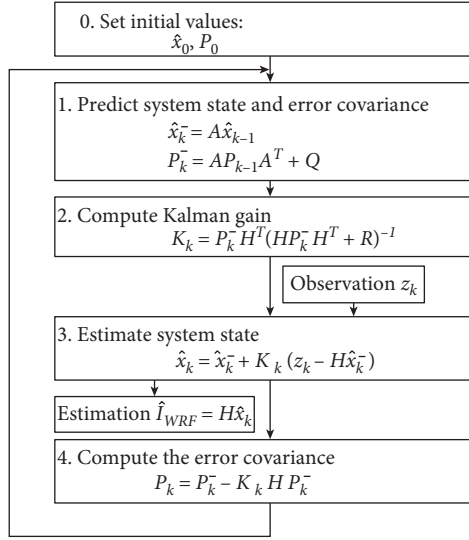
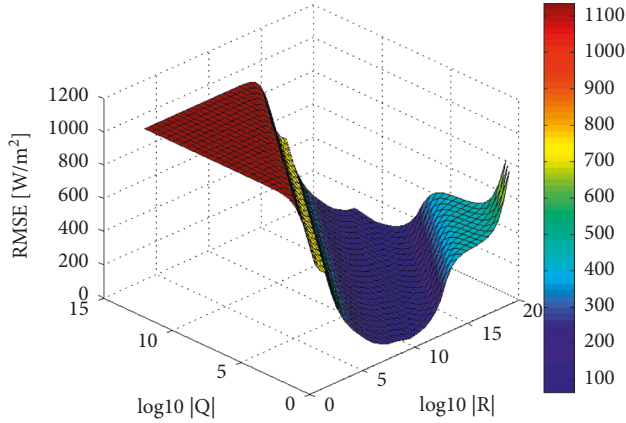


FIGURE 2: Algorithm of Kalman filter.

FIGURE 3: RMSE of the solar GHI intraday forecasting under the different values of covariance matrices R and Q .

the application of Kalman filter to the WRF's results, the evaluated irradiance reduces and approaches the observation data. The method Kalman filter has an effect on the amelioration of the solar global horizontal irradiance forecast shown in this figure.

4. Solar Irradiance Ensemble Prediction

4.1. Ensemble Prediction Method and Forecasting Conditions. Everyday group prediction of solar global horizontal irradiance is controlled with WRF, similar to previous work proposed by Liu et al. [14], with the exception of the application of method Kalman filter, which is a postprocessor for the WRF model. We use similar calculations and circumstances as the latter case in order to contrast [66–71]. The detailed process of the ensemble prediction is stated in the previous research [14]; therefore, we give only the outlines here [72].

The lagged averaged forecast (LAF) which is made up of members with distinct original situation and time is used for

group prediction. Figure 7 shows the chart of the cycle of operation for the ensemble prediction of solar GHI. $M_{i,j}$ - KF indicate the members of the ensemble prediction based on WRF output and Kalman filter, in which i refers to the running day and amounts to the day of the termination of calculation, and j represents the scope of the forecasting day. Hence, $j = 0$ refers to the result of the intraday; $j = 1$ refers to the result of the next-day; and $j = 2$ refers to the results of the 2-day ahead forecasting from the running day. As the figure displayed, GHI of the intraday forecasting in the running day i is predicted based on three members: $M_{i,0}$ - KF, $M_{i-1,1}$ - KF, and $M_{i-2,2}$ - KF. GHI of the next-day forecasting in the running day i is predicted based on two members: $M_{i,1}$ - KF and $M_{i-1,2}$ - KF. GHI of the 2-day ahead forecasting in the running day i is predicted based on one member: $M_{i,2}$ - KF.

The spread of the forecasting members is also defined with the following equation:

$$\text{Spread}_{i,j} = \sqrt{\frac{1}{N-j} \sum_{k=0}^{N-j-1} (\text{GHI}_{i-k,j+k} - \overline{\text{GHI}})^2}, \quad (6)$$

where j equals to 0, 1, and 2; N represents the number of forecasting day in one running, and it is equal to 3 in this work; $N-j$ means the member number of ensemble prediction; $\overline{\text{GHI}}$ is the averaged GHI value of the ensemble members; and $\text{GHI}_{i-k,j+k}$ refers to the predicted GHI value of the member $M_{i-k,j+k}$. This spread serves as the evaluation factors of uncertainty of the forecasting [14].

4.2. Solar Global Horizontal Irradiance Ensemble Prediction.

The certainty of the outcome pointed out for solar global horizontal irradiance prediction is examined in Figure 5 and Table 2. It is found that Bias, RMSE, and CORR, the statistical error indices of $M_{i,0}$ forecasting, are the optimal in those figure and table. In general, in the ensemble prediction method, the ensemble average is selected as the predicted value, brief noted as ensemble mean-KF in this research. Nevertheless, $M_{i,0}$ - KF, which represents the intraday forecasting value based on WRF and Kalman filter, is used as the predicted value in this work, for the reason that the precision of the intraday forecasting is optimum.

4.3. Evaluation Index of Ensemble Prediction.

Figure 8 displays the link in between the distribution within a day prediction and its prediction flaws from the examination throughout the time from September 1 to November 30 2013. Also, the top and bottom peripheries in the prediction interval whose coverage rates are 50 percent, 80 percent, 90 percent, and 95 percent respectively are linked with lines in this chart. These lines are assessed during per 10 W/m^2 in the target spread on the one hand and, on the other hand, are assessed negative and positive errors, respectively. The plotted data gather around the original point of the chart. Meanwhile, the forecasting error values deviate in a wide way with the target spread getting large as figured with the periphery lines of the extents.

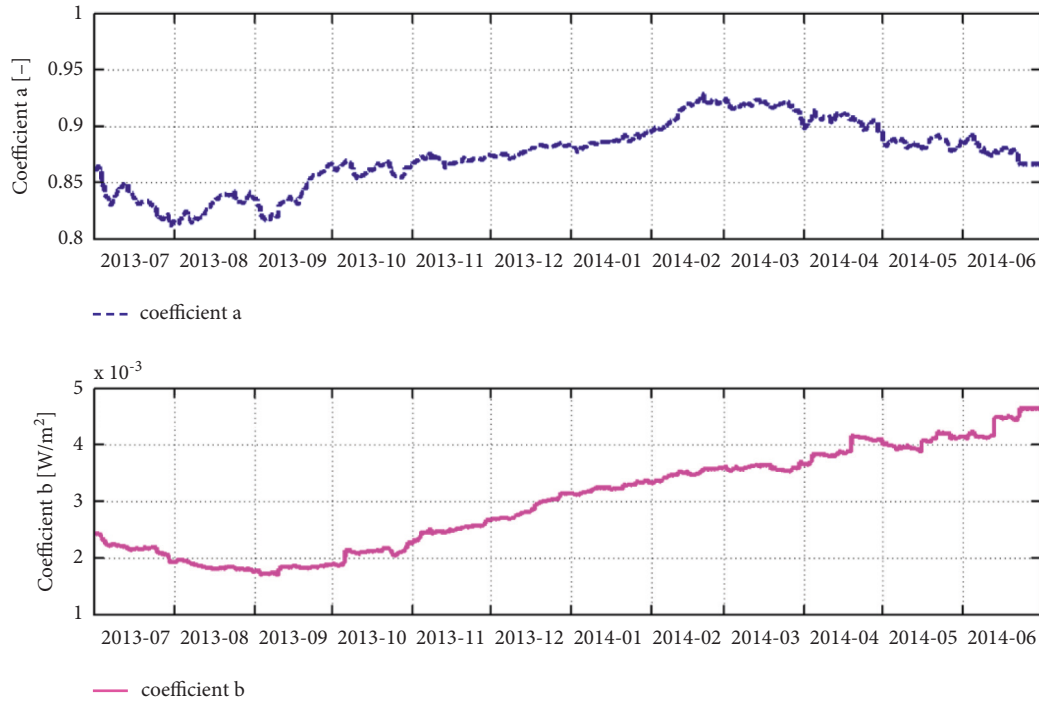


FIGURE 4: Time series of correction coefficients in the method Kalman filter for the intraday forecasting during the period from July 2013 to July 2014.

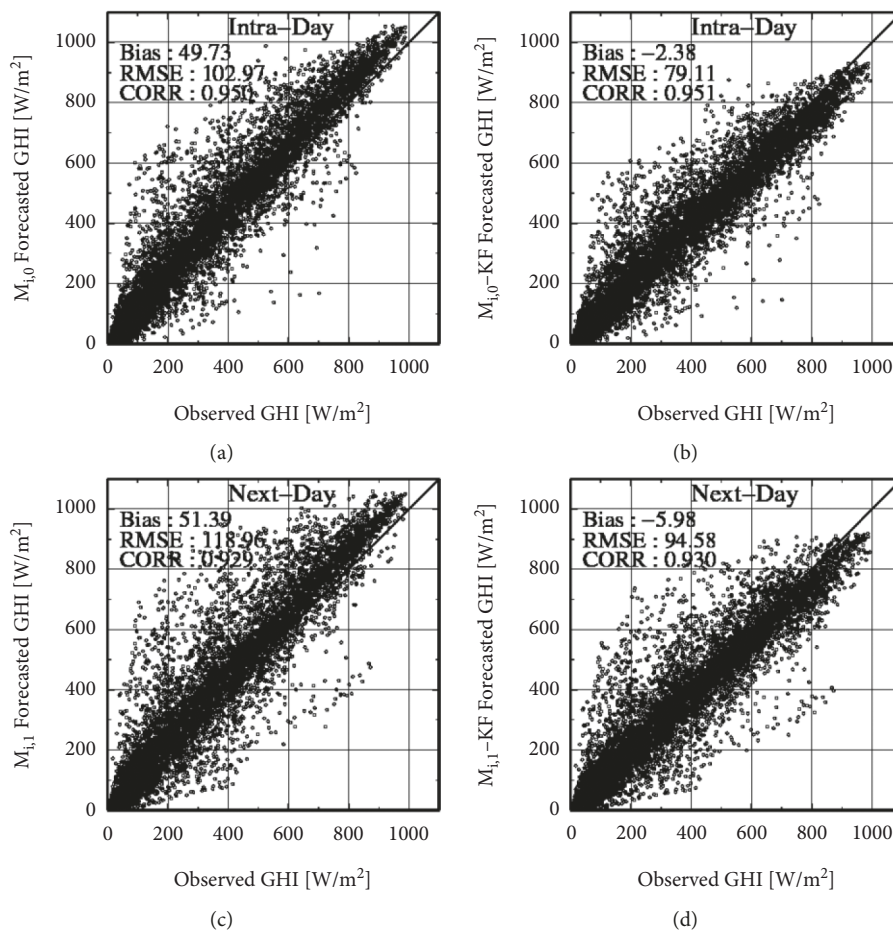


FIGURE 5: Continued.

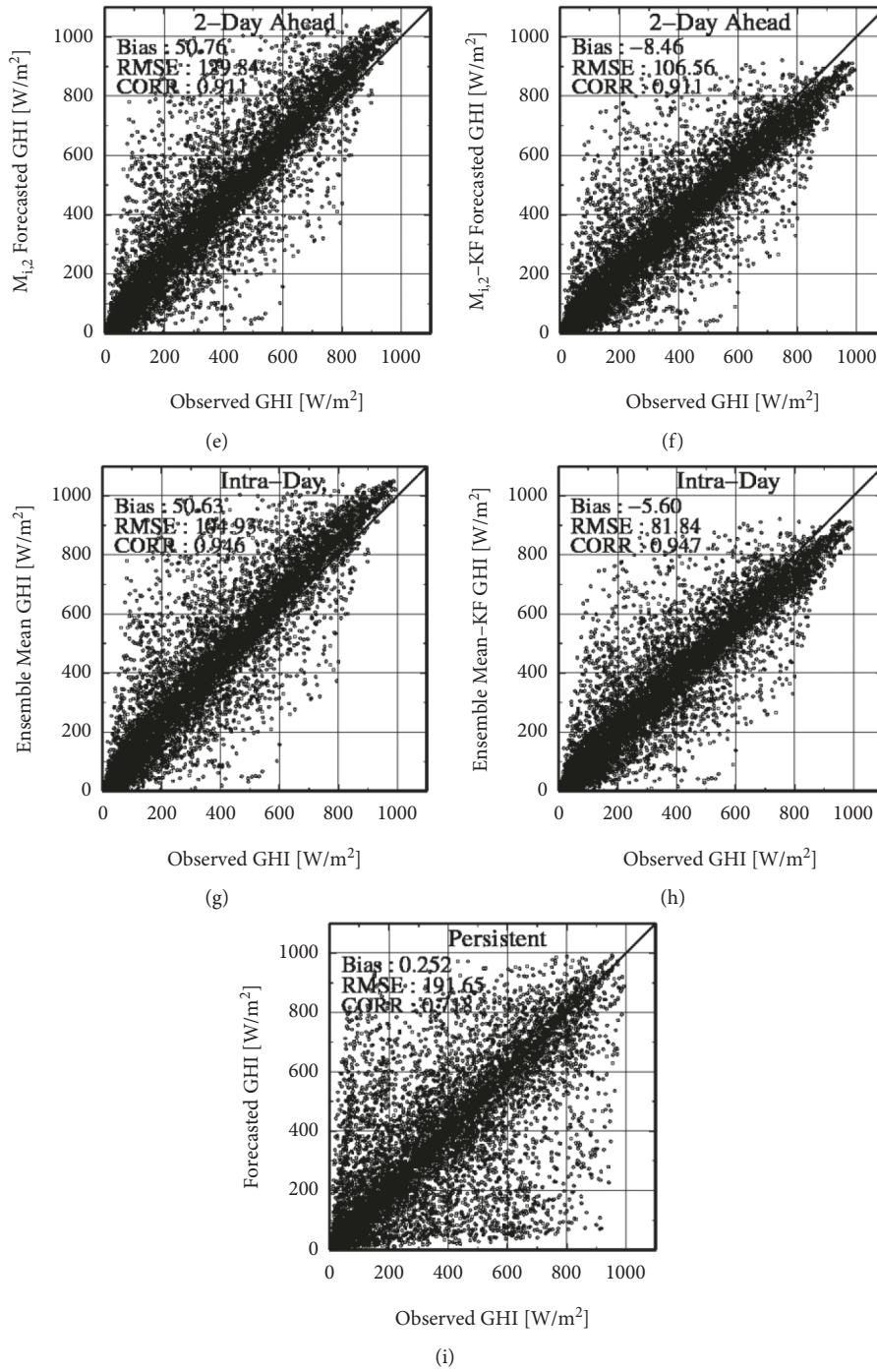


FIGURE 5: Correlation diagrams of the observed GHI and the forecasted data for the intraday prediction, next-day prediction, 2-day ahead prediction, and ensemble mean with the meteorological model WRF only ($M_{i,0}$, $M_{i,1}$, $M_{i,2}$, and ensemble mean), with WRF and post-treatment Kalman filter ($M_{i,0}$ - KF, $M_{i,1}$ - KF, $M_{i,2}$ - KF, and ensemble mean - KF), and the persistent prediction. (a) $M_{i,0}$ prediction, (b) $M_{i,0}$ - KF prediction, (c) $M_{i,1}$ prediction, (d) $M_{i,1}$ - KF prediction, (e) $M_{i,2}$ prediction, (f) $M_{i,2}$ - KF prediction, (g) ensemble mean, (h) ensemble mean - KF, and (i) persistent.

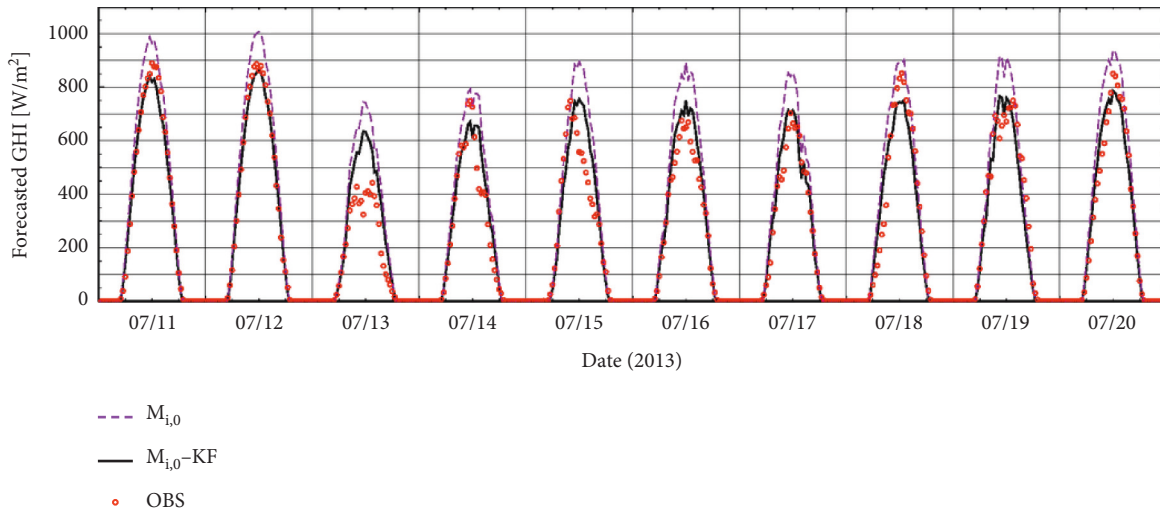


FIGURE 6: Results of intraday prediction of the solar GHI (global horizontal irradiance) by using WRF only $M_{i,0}$, based on WRF and method Kalman filter $M_{i,0} - KF$ and observed one during the period from July 11 to 20 in 2013.

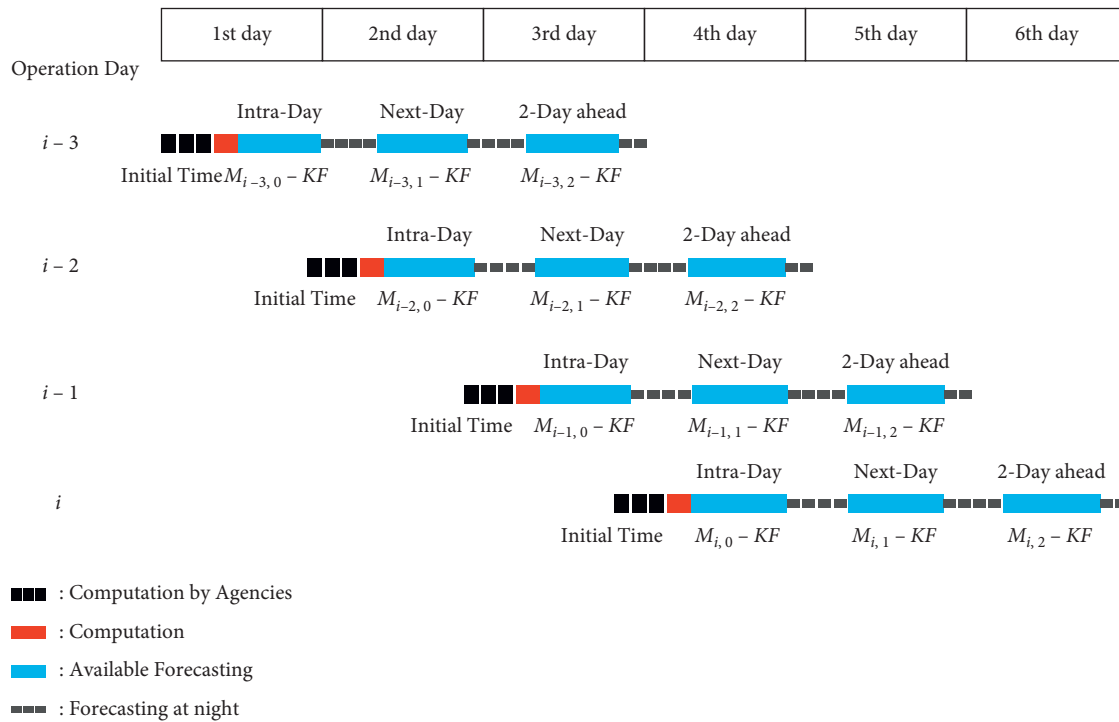


FIGURE 7: Cycle of operation for the solar GHI ensemble prediction based upon model WRF and method Kalman filter.

The periphery lines in the prediction extents are coarse, for the reason that three is the limitation for the ensemble member with the target spread containing random error, which results in the limitation range of the computing environment in this project. The increasement of ensemble members makes contribution to the amelioration of the interval evaluation [73–76].

The distribution of scatter diagrams and the periphery lines of $M_{i,0}$, which is the calculated outcomes with model WRF, deflects to the positive side, because WRF has the tendency to overestimate the solar global horizontal irradiance as explained before. The pure WRF forecasting is

symmetric with respect to the horizontal line 30 W/m^2 . On the other hand, the plots and the periphery lines, with an exception of the lines whose coverage rate is 95 percent, distribute in a symmetrical way relative to the axis of abscissas. This is the result of method Kalman filter, which corrects the overestimating calculation of model WRF.

4.4. Solar Global Horizontal Irradiance Forecasting with Prediction Interval. Every day solar global horizontal irradiance ensemble prediction is performed, and the solar lustrous and its prognosis interval are forethought. Figure 9

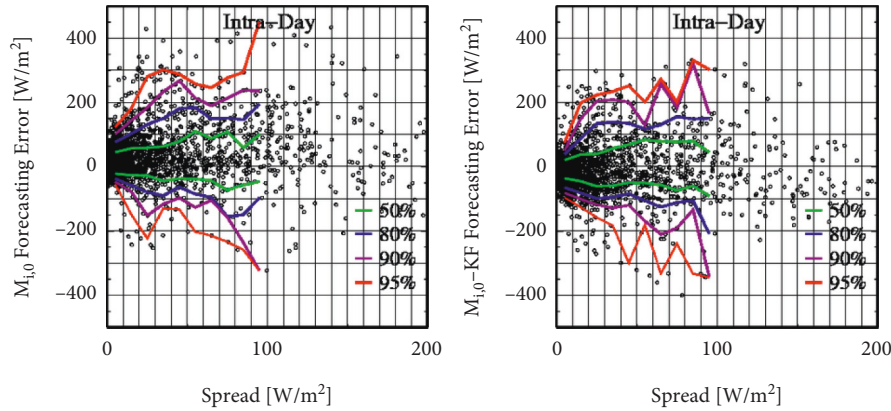


FIGURE 8: Relationship chart between the ensemble spread and solar GHI’s forecasting error for the intraday prediction by using model WRF only $M_{i,0}$, based on WRF and method Kalman filter $M_{i,0} - KF$ during the period from September 1 to November 30 in 2013.

shows the irradiance forecasted with WRF only, and Figure 10 displays the irradiance with model WRF and method Kalman filter. In these charts, the calculated outcomes of the intraday forecasting data are linked up and shown during the time series between December 1 and December 10 2013. By respectively using black full lines and red dot lines in these charts, the data of the predicted irradiance and the data of observed ones are plotted. As a result of the overestimation of model WRF, the outcome of irradiance which is predicted with model WRF is greater than the observed data in Figure 9. On the other hand, the forecasting results with WRF and Kalman filter is suited to the observed data as indicated in Figure 10.

The ensemble spread of the members with model WRF and based on model WRF and method Kalman filter is also displayed by using dashed lines in green in Figures 9(a) and 10(a). The target spread value alters with time; for instance, the target spread on December 6 is not small, while the target spread on December 3 is close to zero in these charts. As the ensemble spread becomes smaller, the predicted GHI values come closer to the observed one.

The top and bottom peripheries in the prediction interval are displayed by using two dashed lines in blue which situate from Figures 9(b)–9(e) and from Figures 10(b)–10(e), whose coverage rates are respectively 50 percent, 80 percent, 90 percent, and 95 percent. For the sake of evaluating the peripheries of the predicted intervals, the top and bottom peripheries in the prediction interval in Figure 8(a) or 8(b) are assessed based on the given rates of nominal coverage and the target spread in Figures 9(a) or 10(a) at first. And, defined as the prediction interval, they are drawn based on the forecasted irradiance. In these charts, accompanied with the decrease of target spread, the interval size, which can be found from the data on December third, is small. On the contrary, the interval size becomes large when the target spread increases, just like the data on December 6. As is

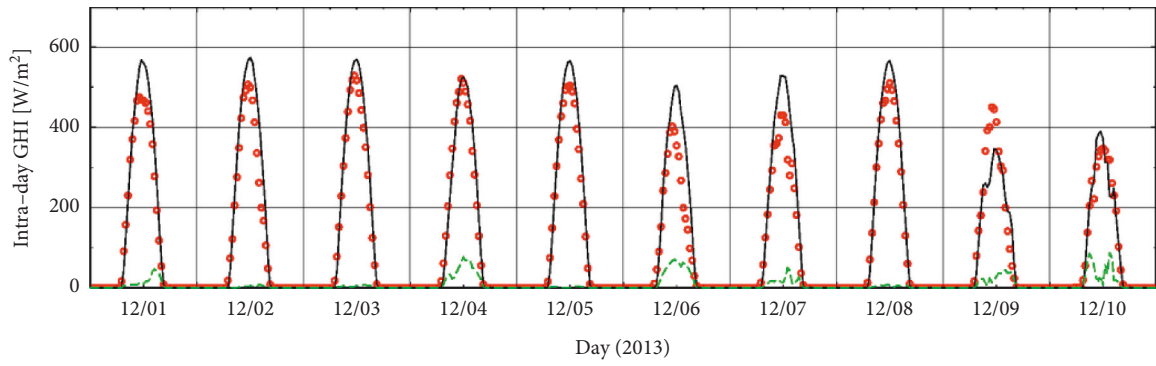
displayed in these charts, the rate of nominal coverage gets large compared with the interval size in proportional way.

Table 3 displays the rate of daily empirical coverage, which refers to the ratio of the actual data number of observed data fallen in the estimated interval, to the total data number within the effective sunshine time, for the intraday solar GHI ensemble prediction during the period from December 1 to 10 in 2013. $M_{i,0}$ represents the predicted result based on model WRF, and $M_{i,0} - KF$ represents the predicted result based on model WRF and method Kalman filter in this table. It is revealed that the rate of empirical coverage is in proportion to the rate of nominal coverage, which is greater than the rate of daily empirical coverage of $M_{i,0}$ and approached by the rate of daily empirical coverage of $M_{i,0} - KF$.

During the period from December 1 to 10 2013, Table 4 shows the daily prediction interval sizes for the intraday solar GHI ensemble prediction. For the size computation, the data at night are refused. It is revealed that the sizes get in proportion to the rates of nominal coverage in this table. The sizes of $M_{i,0} - KF$ forecasting is smaller than the ones of $M_{i,0}$ forecasting.

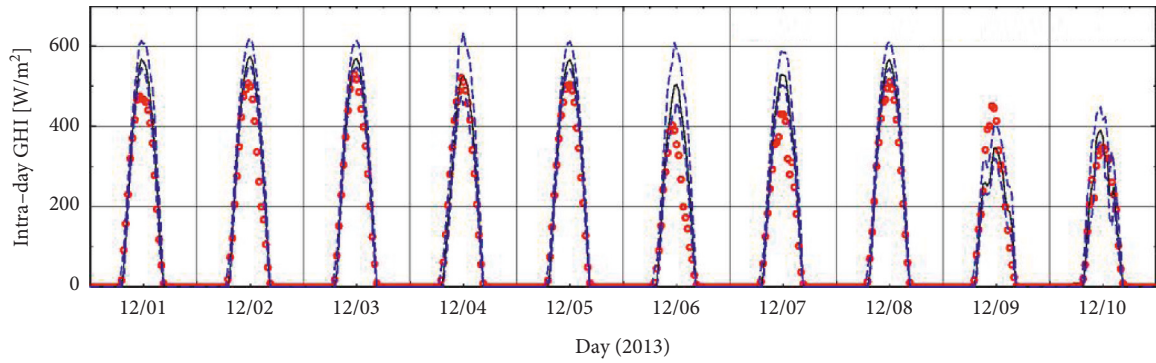
To improve the WRF calculation, solar global horizontal irradiance via Kalman filter is used. Applying it to the ensemble prediction brings about the size of the prognosis interval gradually little and the factual analysis quota rises and closes to the nominal one. It signifies that the amelioration of the forecasting provides a better assessment for prediction interval.

Furthermore, monthly empirical coverage rates and prediction interval sizes from October 2013 to June 2014 are illustrated in Figures 11 and 12. With the application of Kalman filter in improving the solar GHI forecasting, the prediction interval sizes get small, while the rates of empirical coverage add and become near the nominal rates in the long period. It means that the improvement in the forecasting works well for the improvement in the prediction interval estimation.



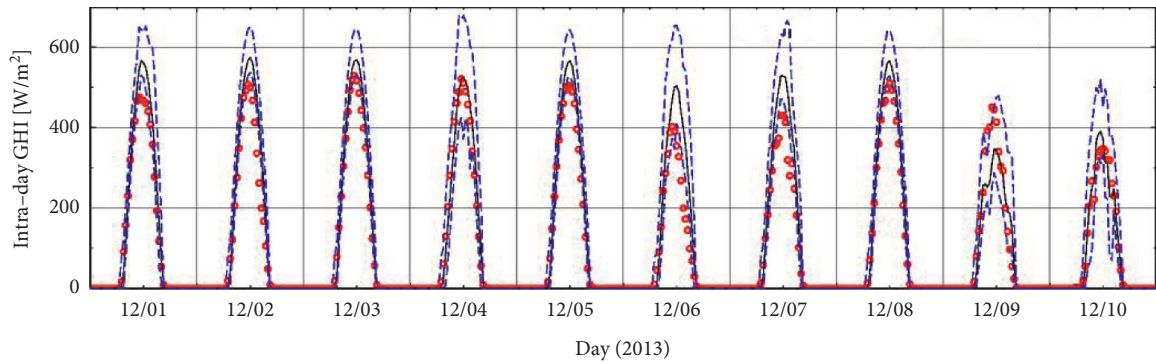
○ OBS
— $M_{i,0}$
- - - $M_{i,0}$ Spread

(a)



○ OBS
— $M_{i,0}$
- - - 50% $M_{i,0}$ Error Interval

(b)



○ OBS
— $M_{i,0}$
- - - 80% $M_{i,0}$ Error Interval

(c)

FIGURE 9: Continued.

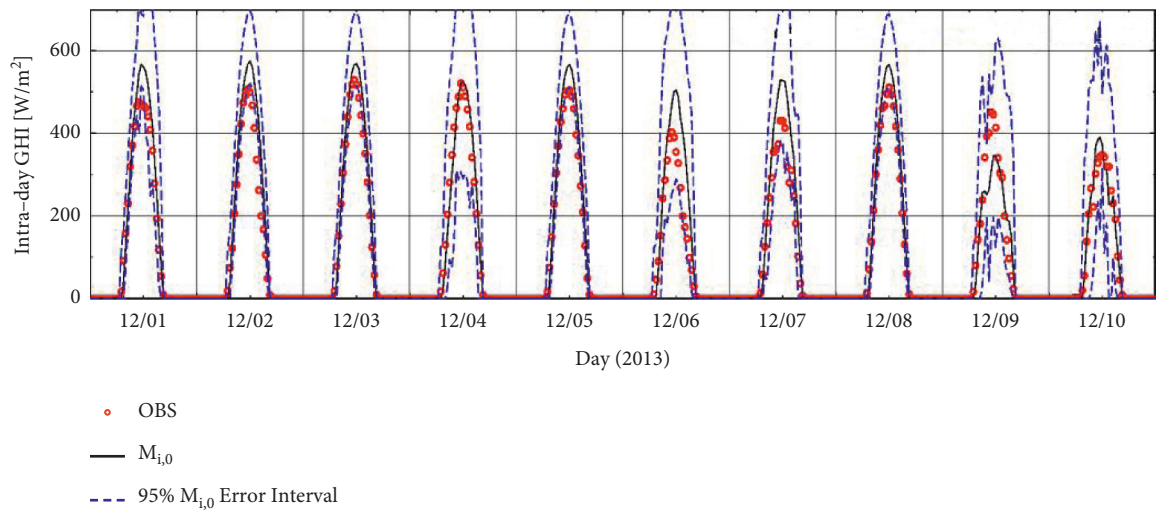
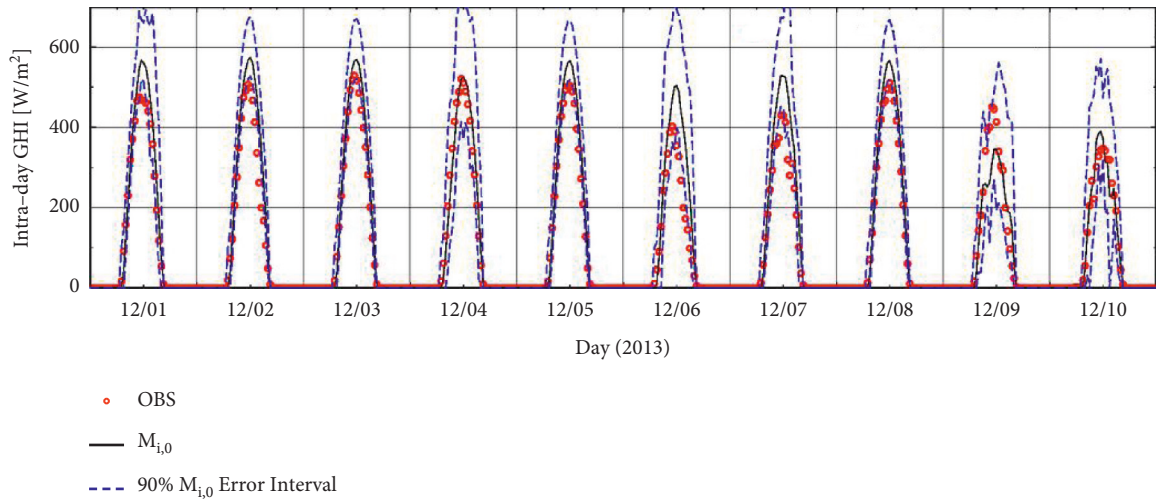


FIGURE 9: Time series of solar GHI intraday prediction by using model WRF only $M_{i,0}$ and its 50%, 80%, 90%, and 95% prediction interval during the period from December 1 to 10 in 2013. (a) $M_{i,0}$ prediction and ensemble spread, (b) $M_{i,0}$ prediction and 50% prediction interval, (c) $M_{i,0}$ prediction and 80% prediction interval, (d) $M_{i,0}$ prediction and 90% prediction interval, and (e) $M_{i,0}$ prediction and 95% prediction interval.

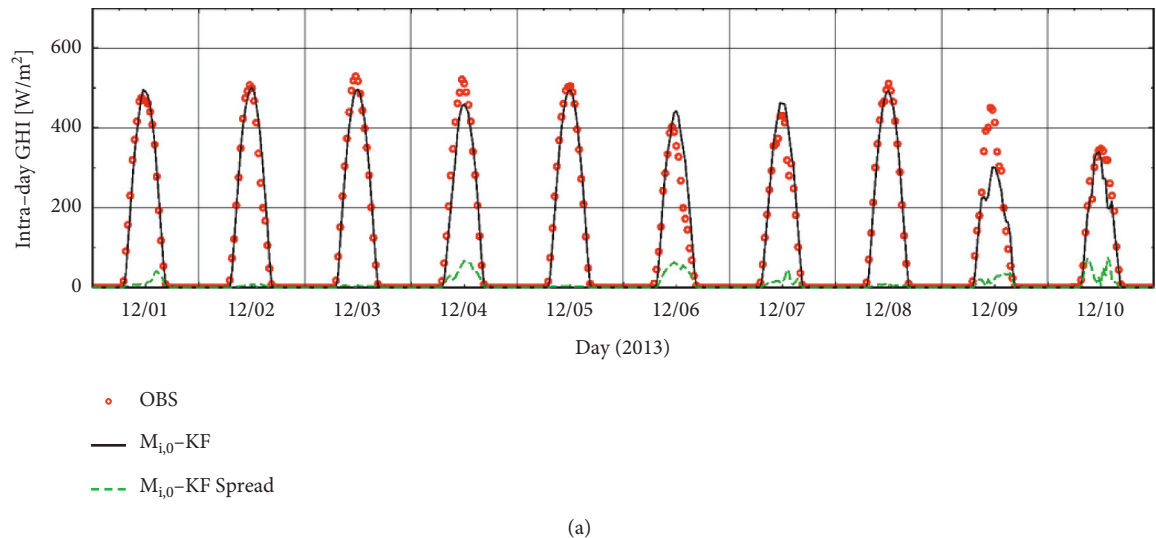
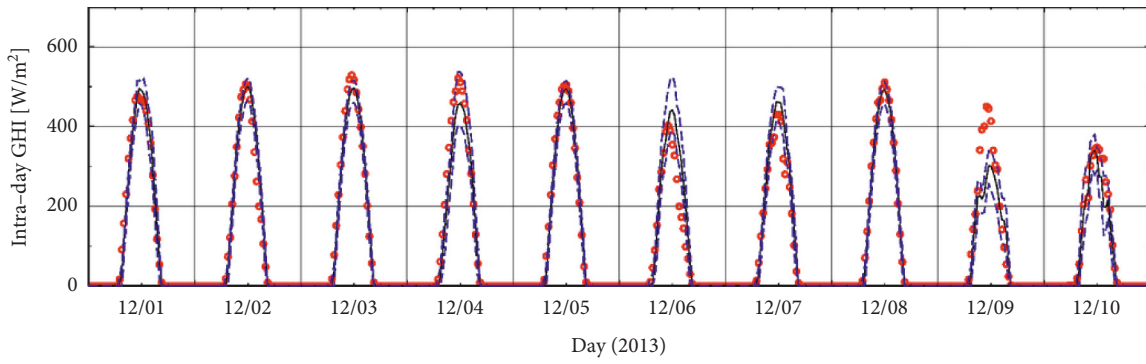
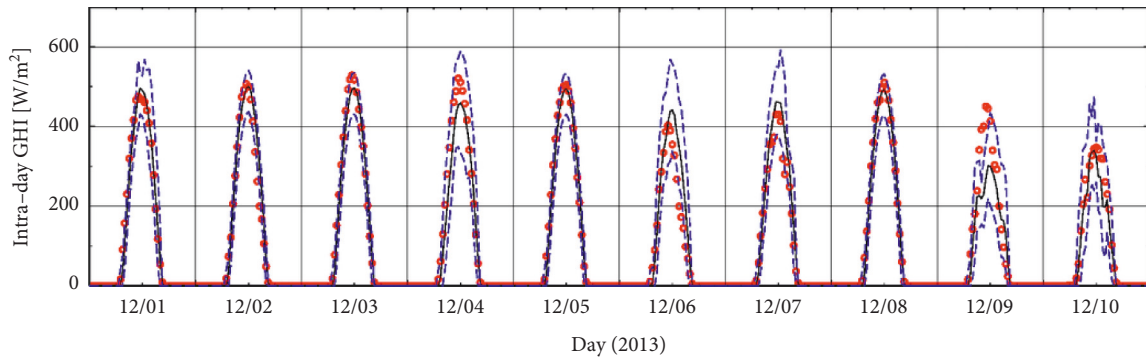


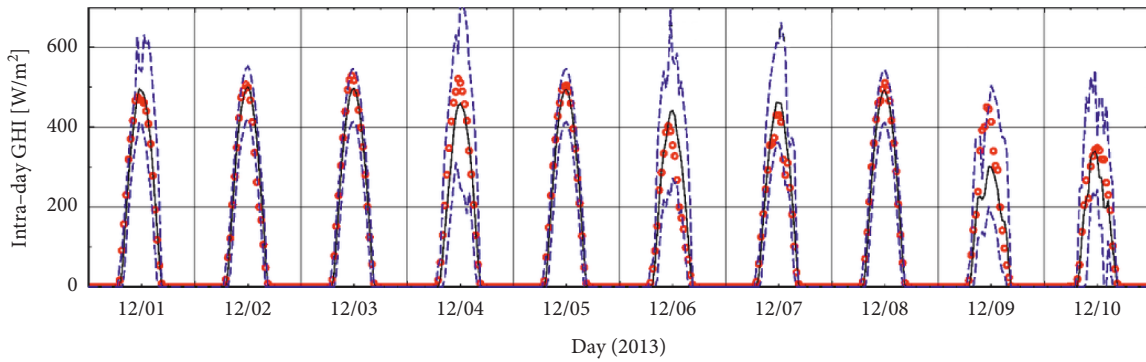
FIGURE 10: Continued.



(b)



(c)



(d)

FIGURE 10: Continued.

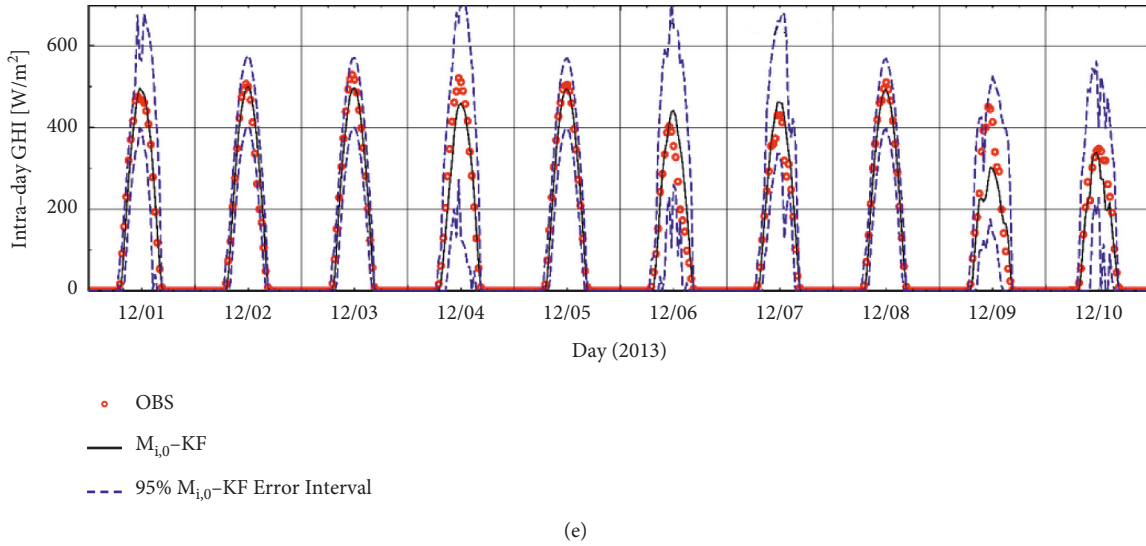


FIGURE 10: Time series of solar GHI intraday prediction $M_{i,0}$ – KF based on model WRF and method Kalman filter, and its 50%, 80%, 90%, and 95% prediction interval during the period from December 1 to 10 in 2013. (a) $M_{i,0}$ – KF prediction and ensemble spread, (b) $M_{i,0}$ – KF prediction and 50% prediction interval, (c) $M_{i,0}$ – KF prediction and 80% prediction interval, (d) $M_{i,0}$ – KF prediction and 90% prediction interval, and (e) $M_{i,0}$ – KF prediction and 95% prediction interval.

TABLE 3: Rates of empirical coverage for the intraday solar GHI prediction with regard to the prediction interval of the ensemble prediction during the period from December 1 to 10th 2013.

Rate of nominal coverage for prediction interval (%)	Forecasting method and member	Rate of empirical coverage for prediction interval [%]										
		12/01	12/02	12/03	12/04	12/05	12/06	12/07	12/08	12/09	12/10	Ave
50	$M_{i,0}$	31.6	10.5	31.6	73.7	26.3	26.3	21.1	26.3	36.8	63.2	34.7
	$M_{i,0}$ – KF	57.9	52.6	42.1	57.9	57.9	47.4	63.1	57.9	36.8	68.4	54.2
80	$M_{i,0}$	63.2	26.3	52.6	89.5	36.8	57.9	36.8	36.8	73.7	94.7	56.8
	$M_{i,0}$ – KF	73.7	78.9	78.9	89.5	84.2	68.4	84.2	89.5	63.1	94.7	80.5
90	$M_{i,0}$	73.7	42.1	57.9	94.7	47.4	57.9	57.9	47.4	89.5	94.7	66.3
	$M_{i,0}$ – KF	84.2	78.9	94.7	94.7	94.7	89.5	94.7	94.7	78.9	94.7	90.0
95	$M_{i,0}$	84.2	47.4	63.2	94.7	52.6	94.7	78.9	47.4	89.5	94.7	74.7
	$M_{i,0}$ – KF	94.7	84.2	94.7	94.7	94.7	94.7	94.7	94.7	89.5	94.7	93.2

TABLE 4: Prediction interval sizes for the intraday solar GHI prediction with regard to the prediction interval of the ensemble prediction during the period from December 1 to 10 in 2013.

Rate of nominal coverage for prediction interval (%)	Prediction method and member	Prediction interval size [W/m ²]										
		12/01	12/02	12/03	12/04	12/05	12/06	12/07	12/08	12/09	12/10	Ave
50	$M_{i,0}$	79.9	65.4	65.4	112.9	65.4	120.9	82.9	65.4	90.8	104.7	85.4
	$M_{i,0}$ – KF	76.7	55.0	55.0	107.9	54.9	109.7	78.3	54.9	91.6	98.9	78.3
80	$M_{i,0}$	155.6	111.8	111.8	231.9	111.8	232.1	164.5	111.7	196.7	208.0	163.6
	$M_{i,0}$ – KF	147.2	99.6	99.6	212.2	99.5	196.9	155.8	99.4	188.4	190.6	148.9
90	$M_{i,0}$	217.0	144.5	144.5	316.4	144.4	304.6	233.3	144.3	287.1	284.4	222.1
	$M_{i,0}$ – KF	208.6	127.1	126.9	328.0	126.9	290.3	223.1	126.8	272.8	279.0	210.9
95	$M_{i,0}$	274.8	171.9	171.9	427.6	171.8	408.2	320.7	171.8	381.3	378.4	287.9
	$M_{i,0}$ – KF	266.8	163.5	163.3	431.1	163.3	398.9	288.6	163.2	328.8	338.1	270.6

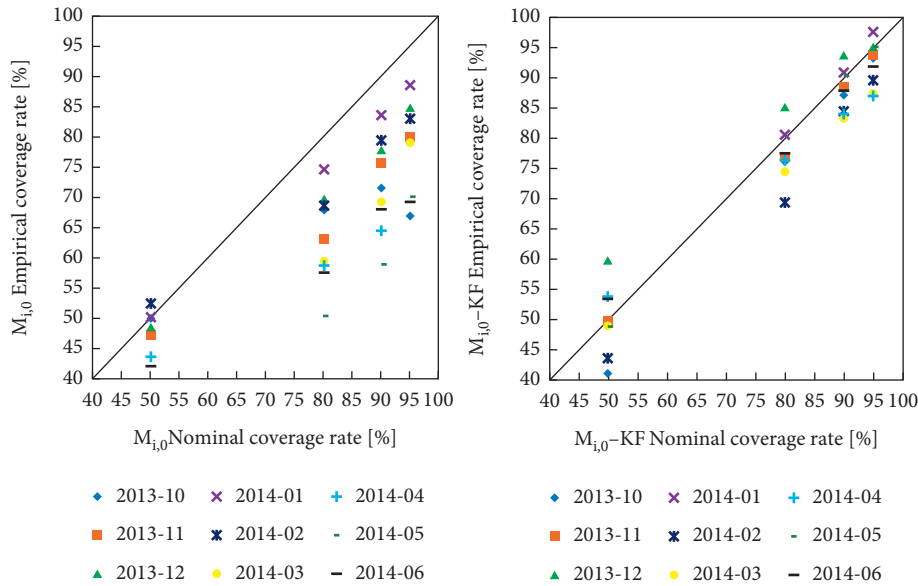


FIGURE 11: Association diagram between monthly rate of empirical coverage and monthly rate of nominal coverage for the intraday solar GHI prediction with regard to the prediction interval of the ensemble prediction during the period from October 2013 to June 2014.

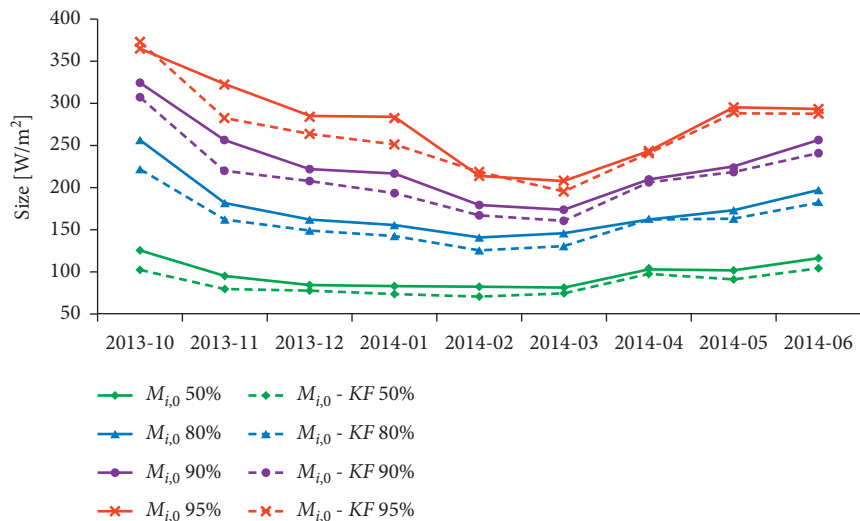


FIGURE 12: Monthly sizes of prediction interval for the intraday solar GHI prediction with regard to the prediction interval of the ensemble prediction during the period from October 2013 to June 2014.

5. Conclusion

This report portraits how solar global horizontal irradiance is accomplished with weather forecast model WRF and collecting data approach Kalman filter. The Kalman filter get rid of aberration of the irradiance calculated with WRF and enhance prognosticating. Also, the ensemble prediction is applied to the forecasting of the solar global horizontal irradiance as well as its prediction interval. The spread of the ensemble forecasting is calculated as a parameter corresponding to the unreliability of the forecasting. And the relation between the spread and the forecasting error is discussed to evaluate the prediction interval. With the prediction interval sizes reducing, its rate of empirical coverage raises and comes close to the nominal

ones by applying the method Kalman filter. In the ensemble prediction, the amelioration through putting the method Kalman filter into use does not fit for the forecasting simply. Meanwhile, it is also suited for the prediction interval assessment. The probabilistic forecasting of solar irradiance presented in this article will be used to predict photovoltaic system generation for electric power grid management and its risk analysis. Compared with other methods, the first highlight of this article is the application of ensemble prediction method to achieve the probabilistic forecasting of solar irradiance. The second highlight is that the Kalman filter is applied into the prediction accuracy of solar irradiance, which is an innovation in solar irradiance prediction research, making the results more exact and reliable.

Further work is to improve the solar GHI prediction by using some interpretable machine learning tools to quantify the parameter importance. The work also seeks to achieve uncertainty quantification of the solar GHI prediction by transferred recurrent neural network for battery calendar health prognostics of energy transportation systems. Furthermore, it is also of great interest to compare and analyze the evaluation of the photovoltaic system installation impact to an electric power grid.

Data Availability

The datasets used and/or analyzed during the current study are available from the corresponding author on reasonable request.

Conflicts of Interest

It is declared by the authors that this article is free of conflicts of interest.

Acknowledgments

The author was supported by the Scientific and Technological Innovation Programs of Higher Education Institutions in Shanxi Province (No. 2019L0983) and Introduction of High-Level Science and Technology Talent Program of Luliang Development Area in Shanxi Province (No. 2019107). The observed solar global horizontal irradiance (Global Horizontal Irradiance, GHI) data used in the work are measured by the Chubu Electric Power Co. Inc. under PV300 project, supported by the Ministry of Economy, Trade and Industry of Japan.

References

- [1] Y. X. Xia, M. H. Feng, S. W. Wang, and C. Lu, "Risk assessment method of rock burst based on the combination of theory and field detection," *Journal of Mining and Strata Control Engineering*, vol. 3, no. 4, Article ID 043017, 2021.
- [2] N. Z. Xu and C. Gao, "Study on the special rules of surface subsidence affected by normal faults," *Journal of Mining and Strata Control Engineering*, vol. 2, no. 1, Article ID 011007, 2020.
- [3] X. Y. Yu, Z. S. Wang, Y. Yang, and X. W. Mao, "Numerical study on the movement rule of overburden in fully mechanized caving mining with thick depth and high mining height," *Journal of Mining and Strata Control Engineering*, vol. 3, no. 1, Article ID 013533, 2021.
- [4] J. D. J. Rubio, "Stability analysis of the modified Levenberg-Marquardt algorithm for the artificial neural network training," *IEEE Transactions on Neural Networks and Learning Systems*, vol. 32, no. 8, pp. 3510–3524, 2021.
- [5] J. D. J. Rubio, E. Lughofer, J. Pieper et al., "Adapting H-infinity controller for the desired reference tracking of the sphere position in the maglev process," *Information Sciences*, vol. 569, pp. 669–686, 2021.
- [6] H. S. Chiang, M. Y. Chen, and Y. J. Huang, "Wavelet-based EEG processing for epilepsy detection using fuzzy entropy and associative petri net," *IEEE Access*, vol. 7, pp. 103255–103262, 2019.
- [7] J. D. J. Rubio, M. A. Islas, G. Ochoa, D. R. Cruz, E. Garcia, and J. Pacheco, "Convergent newton method and neural network for the electric energy usage prediction," *Information Sciences*, vol. 585, pp. 89–112, 2022.
- [8] D. M. Vargas, "Superpixels extraction by an Intuitionistic fuzzy clustering algorithm," *Journal of Applied Research and Technology*, vol. 19, no. 2, pp. 140–152, 2021.
- [9] A. López González, J. A. Meda Campaña, E. G. Hernández Martínez, and P. P. Contro, "Multi robot distance based formation using parallel genetic algorithm," *Applied Soft Computing*, vol. 86, Article ID 105929, 2020.
- [10] E. Lorenz, J. Hurka, D. Heinemann, and H. G. Beyer, "Irradiance forecasting for the power prediction of grid-connected photovoltaic systems," *Ieee Journal of Selected Topics in Applied Earth Observations and Remote Sensing*, vol. 2, no. 1, pp. 2–10, 2009.
- [11] J. Hashimoto and T. Kobayashi, "Solar spectral irradiance model for forecast of photovoltaic power generation," *Japanese Journal of Multiphase Flow*, vol. 25, no. 3, pp. 229–236, 2011.
- [12] M. Diagne, M. David, P. Lauret, J. Boland, and N. Schmutz, "Review of solar irradiance forecasting methods and a proposition for small-scale insular grids," *Renewable and Sustainable Energy Reviews*, vol. 27, pp. 65–76, 2013.
- [13] M. G. De Giorgi, M. Malvoni, and P. M. Congedo, "Comparison of strategies for multi-step ahead photovoltaic power forecasting models based on hybrid group method of data handling networks and least square support vector machine," *Energy*, vol. 107, no. 15, pp. 360–373, 2016.
- [14] Y. Liu, S. Shimada, J. Yoshino, T. Kobayashi, K. Furuta, and Y. Miwa, "Ensemble forecasting of solar irradiance by applying a mesoscale meteorological model," *Solar Energy*, vol. 136, no. 15, pp. 597–605, 2016.
- [15] W. Zhu and Y. H. Teng, "Study on the safety and mining influence of fully-mechanized caving mining with ultrathick seam under barrier lake," *Journal of Mining and Strata Control Engineering*, vol. 3, no. 1, Article ID 013525, 2021.
- [16] W. C. Zhu, L. L. Niu, S. H. Li, and S. Li, "Creep-impact test of rock: status-of-the-art and prospect," *Journal of Mining and Strata Control Engineering*, vol. 1, no. 1, Article ID 013003, 2019.
- [17] J. P. Zuo, M. L. Yu, S. Y. Hu et al., "Experimental investigation on fracture mode of different thick rock strata," *Journal of Mining and Strata Control Engineering*, vol. 1, no. 1, Article ID 013007, 2019.
- [18] K. G. Jiang, L. Wang, S. S. Chi, T. Wei, and C. Jiang, "Boltzmann function prediction model coupled with the correction of inflection point offset and its parameter inversion method," *Journal of Mining and Strata Control Engineering*, vol. 3, no. 2, Article ID 023527, 2021.
- [19] H. P. Kang, "Spatial scale analysis on coalmining and strata control technologies," *Journal of Mining and Strata Control Engineering*, vol. 22, 023538.
- [20] Y. Li and G. Du, "Reasonable width of narrow coal pillars in roadway driving with gas drainage hole," *Journal of Mining and Strata Control Engineering*, vol. 2, no. 1, Article ID 013007, 2020.
- [21] Z. J. Jiang, B. Sun, Y. Ping, and Z. D. Zhu, "Experimental on dynamic response characteristics of rock based on large diameter SHPB," *Journal of Mining and Strata Control Engineering*, vol. 3, no. 4, Article ID 043021, 2021.
- [22] H. P. Kang, "Temporal scale analysis on coal mining and strata control technologies," *Journal of Mining and Strata Control Engineering*, vol. 3, no. 1, Article ID 013538, 2021.
- [23] J. K. Li and H. Wang, "Ground support of interbedded rock roof in a deep roadway with fully-anchored cables," *Journal of*

- Mining and Strata Control Engineering*, vol. 2, no. 3, Article ID 033036, 2020.
- [24] J. H. Li, H. J. Li, Z. C. Li, and Z. Q. Wu, "Research on river dike failure of short-distance coal seams mining under Hunchun river," *Journal of Mining and Strata Control Engineering*, vol. 2, no. 1, Article ID 013538, 2020.
- [25] Y. X. Xia, C. Lu, G. Y. Yang et al., "Experimental study on axial fracture cutting and fracturing of abrasive jet in hard roof hole," *Journal of Mining and Strata Control Engineering*, vol. 2, no. 3, Article ID 033522, 2020.
- [26] B. Xiao, Y. X. Wang, Z. X. Wang, and H. Yi, "Experimental on optimization of gangue particle size gradation in solid filling mining," *Journal of Mining and Strata Control Engineering*, vol. 4, no. 1, Article ID 013516, 2022.
- [27] G. G. Xiao and W. B. Yao, "Law of pressure behavior of shallow buried coal seam in the gully terrain of madiliang coal mine," *Journal of Mining and Strata Control Engineering*, vol. 3, no. 4, Article ID 043023, 2021.
- [28] J. L. Xu, D. Y. Xuan, W. B. Zhu, and X. Z. Wang, "Partial backfilling coal mining technology based on key strata control," *Journal of Mining and Strata Control Engineering*, vol. 1, no. 1, Article ID 013504, 2019.
- [29] A. Rincón, O. Jorba, J. M. Baldasano, and L. Delle Monache, "Assessment of short-term irradiance forecasting based on post-processing tools applied on WRF meteorological simulations," in *Proceedings of the ES1002: Workshop March*, Barcelona, Spain, 2011.
- [30] R. A. Verzijlbergh, P. W. Heijnen, S. R. De Roode, A. Los, and H. J. Jonker, "Improved model output statistics of numerical weather prediction based irradiance forecasts for solar power applications," *Solar Energy*, vol. 118, no. 16, pp. 634–645, 2015.
- [31] E. Lorenz and D. Heinemann, "Prediction of solar irradiance and photovoltaic power," *Comprehensive Renewable Energy*, vol. 1, pp. 239–292, 2012.
- [32] M. Pierro, F. Bucci, C. Cornaro et al., "Model output statistics cascade to improve day ahead solar irradiance forecast," *Solar Energy*, vol. 117, no. 14, pp. 99–113, 2015.
- [33] S. Baran and A. Möller, "Bivariate ensemble model output statistics approach for joint forecasting of wind speed and temperature," *Meteorology and Atmospheric Physics*, vol. 129, no. 1, pp. 99–112, 2017.
- [34] M. Homleid, "Diurnal corrections of short term surface temperature forecasts using the Kalman filter," *Weather and Forecasting*, vol. 10, no. 4, pp. 689–707, 1995.
- [35] J. R. Porto de Carvalho, E. D. Assad, and H. S. Pinto, "Kalman filter and correction of the temperatures estimated by PRECIS model," *Atmospheric Research*, vol. 102, pp. 218–226, 2011.
- [36] L. D. Monache, J. Wilczak, S. Mckeen et al., "A kalman-filter bias correction method applied to deterministic, ensemble averaged and probabilistic forecasts of surface ozone," *Tellus B: Chemical and Physical Meteorology*, vol. 60, no. 2, pp. 238–249, 2008.
- [37] G. Galanis, P. Louka, P. Katsafados, I. Pytharoulis, and G. Kallos, "Applications of kalman filters based on non-linear functions to numerical weather predictions," *Annales Geophysicae*, vol. 24, no. 10, pp. 2451–2460, 2006.
- [38] F. Cassola and M. Burlando, "Wind speed and wind energy forecast through kalman filtering of numerical weather prediction model output," *Applied Energy*, vol. 99, pp. 154–166, 2012.
- [39] S. Pelland, G. Galanis, and G. Kallos, "Solar and photovoltaic forecasting through post-processing of the global environmental multiscale numerical weather prediction model," *Progress in Photovoltaics: Research and Applications*, vol. 21, no. 3, pp. 284–296, 2013.
- [40] M. Diagne, M. David, J. Boland, N. Schmutz, and P. Lauret, "Post-processing of solar irradiance forecasts from WRF model at reunion Island," *Solar Energy*, vol. 105, no. 13, pp. 99–108, 2014.
- [41] A. Rincón, O. Jorba, M. Frutos, L. Alvarez, F. P. Barrios, and J. A. González, "Bias correction of global irradiance modelled with weather and research forecasting model over Paraguay," *Solar Energy*, vol. 170, no. 8, pp. 201–211, 2018.
- [42] R. E. Kalman, "A new approach to linear filtering and prediction problems," *Journal of Basic Engineering*, vol. 82, no. 1, pp. 35–45, 1960.
- [43] W. C. Skamarock, J. B. Klemp, J. Dudhia et al., "A description of the advanced research WRF version 3," University Corporation for Atmospheric Research, Boulder, CO, USA, NCAR Technical Note NCAR/TN-475 + STR, 2008.
- [44] D. Heinemann, E. Lorenz, and M. Girodo, *Solar Global Horizontal Irradiance Forecasting for the Management of Solar Energy systems. Energy and Semiconductor Research Laboratory, Energy Meteorology Group*, Oldenburg University, Oldenburg, Germany, 2006.
- [45] Y. Che, X. Peng, L. Delle Monache, T. Kawaguchi, and F. Xiao, "A wind power forecasting system based on the weather research and forecasting model and kalman filtering over a wind-farm in Japan," *Journal of Renewable and Sustainable Energy*, vol. 8, no. 1, Article ID 013302, 2016.
- [46] Y. P. Li, F. Cui, W. H. Yang, and C. X. Q. Wei, "Dynamic migration law and its control of roof in fully mechanized top coal caving mining in extremely steep and thick coal seams," *Journal of Mining and Strata Control Engineering*, vol. 2, no. 4, Article ID 043538, 2020.
- [47] Y. X. Liu, M. S. Gao, H. S. Zhao, S. L. He, Z. G. Li, and Z. C. Zhang, "Detection of overlying rock structure and identification of key stratum by drilling and logging technology," *Journal of Mining and Strata Control Engineering*, vol. 2, no. 2, Article ID 023038, 2020.
- [48] J. Y. Li, L. Wang, K. G. Jiang, and C. Q. Teng, "Parameter inversion method of probability integral model based on improved wolves algorithm," *Journal of Mining and Strata Control Engineering*, vol. 3, no. 1, Article ID 017038, 2021.
- [49] S. Shimada, Y. Liu, H. Xia et al., "Accuracy of solar global horizontal irradiance simulation using the WRF-ARW model," *Solar Energy*, vol. 38, no. 5, pp. 41–48, 2012.
- [50] G. L. Mellor and T. Yamada, "Development of a turbulence closure model for geophysical fluid problems," *Reviews of Geophysics*, vol. 20, no. 4, p. 851, 1982.
- [51] Z. I. Janjic, "Comments on development and evaluation of a convection scheme for use in climate models," *Journal of the Atmospheric Sciences*, vol. 57, no. 21, p. 3686, 2000.
- [52] J. Dudhia, S. Y. Hong, and K. S. Lim, "A new method for representing mixed-phase particle fall speeds in bulk microphysics parameterizations," *Journal of the Meteorological Society of Japan*, vol. 86, pp. 33–44, 2008.
- [53] J. Dudhia, "Numerical study of convection observed during the winter monsoon experiment using a mesoscale two-dimensional model," *Journal of the Atmospheric Sciences*, vol. 46, no. 20, pp. 3077–3107, 1989.
- [54] E. J. Mlawer, S. J. Taubman, P. D. Brown, M. J. Iacono, and S. A. Clough, "Radiative transfer for inhomogeneous atmospheres: RRTM, a validated correlated-*k* model for the long wave," *Journal of Geophysical Research: Atmospheres*, vol. 102, pp. 16663–16682, 1997.

- [55] M. F. Cai, "Key theories and technologies for surrounding rock stability and ground control in deep mining," *Journal of Mining and Strata Control Engineering*, vol. 2, no. 3, Article ID 033037, 2020.
- [56] Y. F. Cai, X. J. Li, W. N. Deng, W. Xiao, and W. K. Zhang, "Simulation of surface movement and deformation rules and detriment key parameters in high-strength mining," *Journal of Mining and Strata Control Engineering*, vol. 2, no. 4, Article ID 043511, 2020.
- [57] D. F. Yang, Y. J. Zhang, S. Wang, C. H. Niu, and J. L. Chai, "Analysis of the influence of hidden fault dip angle on ground pressure behavior in shallow seam roof," *Journal of Mining and Strata Control Engineering*, vol. 2, no. 4, Article ID 043038, 2020.
- [58] W. Z. Ma, X. M. Zhou, and S. Tan, "Study on failure characteristics of coal seam floor above confined water: a case study of shanxi yitang coal mine," *Journal of Mining and Strata Control Engineering*, vol. 2, no. 3, Article ID 033011, 2020.
- [59] K. Fan, "Sudden deformation characteristic and cuttingroof support technology for double-used roadways in longtan Mine," *Journal of Mining and Strata Control Engineering*, vol. 2, no. 3, Article ID 033032, 2020.
- [60] M. Kunitsugu, "Statistical guidance systems using Kalman filter technique," *Meteorological Society of Japan*, vol. 5, pp. 7–21, 1997.
- [61] P. Kim and L. Huh, *Kalman Filter for Beginners with Matlab Examples*, CreateSpace Independent Publishing Platform, Scotts Valley, CA, USA, 2011.
- [62] F. Q. Gao, "Use of numerical modeling for analyzing rock mechanic problems in underground coal mine practices," *Journal of Mining and Strata Control Engineering*, vol. 1, no. 1, Article ID 013004, 2019.
- [63] Y. L. Bi, X. L. Li, and N. Guo, "Spatial heterogeneity of vegetation and soil nutrients induced by the open-pit mining in eastern grassland of China," *Journal of Mining and Strata Control Engineering*, vol. 2, no. 4, Article ID 047036, 2020.
- [64] S. Fan, Y. Wang, S. Cao, B. Zhao, T. Sun, and P. Liu, "A deep residual neural network identification method for uneven dust accumulation on photovoltaic (PV) panels," *Energy*, vol. 239, Article ID 122302, 2022.
- [65] S. Wang, K. Zhang, L. Chao et al., "Exploring the utility of radar and satellite-sensed precipitation and their dynamic bias correction for integrated prediction of flood and landslide hazards," *Journal of Hydrology*, vol. 603, Article ID 126964, 2021.
- [66] F. Q. Gao, "Influence of hydraulic fracturing of strong roof on mining-induced stress-insight from numerical simulation," *Journal of Mining and Strata Control Engineering*, vol. 3, no. 2, Article ID 023032, 2021.
- [67] B. L. Zhang, B. T. Shen, J. H. Zhang, and X. G. Zhang, "Experimental study of edge-opened cracks propagation in rocklike materials," *Journal of Mining and Strata Control Engineering*, vol. 2, no. 3, Article ID 033035, 2020.
- [68] J. Chai, Y. Y. B. Ou, and D. D. Zhang, "Crackdetection method in similar material models based on DIC," *Journal of Mining and Strata Control Engineering*, vol. 2, no. 2, Article ID 023015, 2020.
- [69] K. Zhang, S. Wang, H. Bao, and X. Zhao, "Characteristics and influencing factors of rainfall-induced landslide and debris flow hazards in Shaanxi Province, China," *Natural Hazards and Earth System Sciences*, vol. 19, no. 1, pp. 93–105, 2019.
- [70] K. Zhang, A. Ali, A. Antonarakis et al., "The sensitivity of north american terrestrial carbon fluxes to spatial and temporal variation in soil moisture: an analysis using radar-derived estimates of root-zone soil moisture," *Journal of Geophysical Research. Biogeosciences*, vol. 124, no. 11, pp. 3208–3231, 2019.
- [71] Y. Zhang, Y. He, H. Wang, L. Sun, and Y. Su, "Ultra-Broadband mode size converter using on-chip metamaterial-based luneburg lens," *ACS Photonics*, vol. 8, no. 1, pp. 202–208, 2021.
- [72] Q. C. Zhao, B. J. Fu, and J. Yin, "Deformation mechanism and control technology of the surrounding rock of the floor roadway under the influence of mining," *Advances in Civil Engineering*, vol. 2020, Article ID 661303, 23115 pages, 2020.
- [73] C. Jia and C. C. Hu, "Instability mechanism and control technology of longwall entries driving along the gob in a thick coal seam," *Journal of Mining and Strata Control Engineering*, vol. 2, no. 4, Article ID 043535, 2020.
- [74] X. Fu and R. F. Wang, "Cooperative self-adaptive control model of fluid feeding system and hydraulic supports in working face," *Journal of Mining and Strata Control Engineering*, vol. 2, no. 3, Article ID 036031, 2020.
- [75] J. Wang and X. L. Wang, "Seepage characteristic and fracture development of protected seam caused by mining protecting strata," *Journal of Mining and Strata Control Engineering*, vol. 3, no. 3, Article ID 033511, 2021.
- [76] X. W. Zang, J. H. Xu, Z. B. Liu, and L. Sun, "Mechanical response and deformation law of weak interbedded mudstone under different loading paths," *Journal of Mining and Strata Control Engineering*, vol. 3, no. 4, Article ID 043022, 2021.